Study of the reaction $\pi^- p \to n K_s^0 K_s^0$ at 6.0 and 7.0 GeV/c

V. A. Polychronakos†, N. M. Cason, J. M. Bishop, N. N. Biswas, V. P. Kenney, D. S. Rhines††, R. C. Ruchti, W. D. Shephard, and M. J. Stangl
University of Notre Dame, Notre Dame, Indiana 46556

J. M. Watson
Argonne National Laboratory, Argonne, Illinois 60439
(Received 31 July 1978)

The $K_s^0 K_s^0$ system produced in the reaction $\pi^- p \to n K_s^0 K_s^0$ at 6.0 and 7 0 GeV/c has been studied utilizing the ANL 1.5-m streamer-chamber facility. A 400 000-photograph exposure yielded 5096 unweighted $n K_s^0 K_s^0$ events. The cross section for this reaction was determined to be 9.6 ± 1.3 μb at 6.0 GeV/c and 8.7 ± 1.1 μb at 7.0 GeV/c. The decay angular distributions were parametrized in terms of moments of the spherical harmonics. The $\langle Y_4^0 \rangle$ moment was fitted to interfering Breit-Wigner amplitudes for the f and f' mesons. Using this fit, the branching ratio $R = \Gamma(f \to K\bar{K})/\Gamma(f \to \text{all})$ was found to be (2.3 ± 0.8)%. An energy-independent production-amplitude analysis revealed an enhancement in the S-wave amplitude near 1300 MeV. The properties of the S-wave enhancement are discussed and compared with those observed in other recent experiments. Extrapolated cross sections for the reaction $\pi\pi \to K_s^0 K_s^0$ are presented. We find a cross section considerably below the S-wave unitarity limit in the S^* region.

I. INTRODUCTION

We present the analysis of an experiment studying the $K_S^0 K_S^0$ system produced peripherally in the reaction

$$\pi^- p \to n K_S^0 K_S^0 \tag{1}$$

at 6.0 and 7.0 GeV/c. The experiment was performed at the Argonne National Laboratory Zero Gradient Synchrotron (ZGS) utilizing the 1.5-m streamer-chamber facility.

Some results of this experiment have been reported previously.[1-3] Most of the work reported from earlier experiments on the $K_S^0 K_S^0$ system, produced either inclusively or in the final state $n K_S^0 K_S^0$, has been from bubble chambers.[4-7] In these experiments, low statistics made study of the rather complex $K_S^0 K_S^0$ spectrum quite difficult. Earlier spark-chamber experiments including a series of experiments at CERN by Beusch *et al.*,[8,9] as well as an older Notre Dame–ANL experiment,[10-12] had much higher statistics but were limited by geometrical acceptance and trigger biases. A recent CERN spark-chamber experiment[13] performed at 8.9 GeV/c is comparable in statistics to this experiment, and results from that experiment will be compared to our data when appropriate. The streamer chamber was chosen for the present experiment because it combines the good resolution and 4π geometry of the bubble chamber with the trigger capability and therefore high statistical accuracy of the spark chamber.

The fact that the two observed K_S^0's are indistinguishable pseudoscalars severely restricts the quantum numbers of any resonance decaying into a $K_S^0 K_S^0$ system. These quantum numbers are $J^P = \text{even}^+$, $I^G = 0^+$ or 1^-, and $C = +1$. Table I lists all the possible states of the $K_S^0 K_S^0$ system up to $l = 4$ as well as the known resonances that can couple to the corresponding quantum states. This table reveals the importance of the $K_S^0 K_S^0$ system as a source of information on the long-debated scalar-meson nonet as well as the better-known tensor-meson nonet without the complications of additional parameters introduced by the contributions of P and F waves. The study of these two SU(3) multiplets was the primary goal of this experiment.

II. EXPERIMENTAL APPARATUS

Some of the experimental details have already been published[1] but are repeated here for completeness. The performance of the ANL streamer chamber has been extensively covered in the literature.[14-17]

The streamer chamber is located at the end of beam 22, a secondary beam of the ZGS external proton beam 1 (EPB-1). Beam 22 is a high-momentum unseparated beam with 0.4-msr transport acceptance at a 1.5° production angle. The momentum spread of the beam was 1.5%. The beam spot at the final focal plane was 9 mm (vertical) × 12 mm (horizontal) full width at half maximum.

TABLE I. Possible states of the $K_S^0 K_S^0$ system.

J^P	I^G	Corresponding resonance
0^+	0^+	S^*
	1^-	δ
2^+	0^+	f°
	1^-	A_2°
4^+	0^+	h
	1^-	?

The liquid-hydrogen (LH_2) target consisted of a cyclindrical flask 7.5 cm long and 5 cm in diameter with spherically shaped cups at the two ends made of 0.005-in.-thick Mylar. The single feed line was also made from 0.005-in. Mylar. The flask and the vent line were enclosed in an epoxy-coated polyvinyl chloride (PVC) foam vacuum jacket for thermal insulation. The LH_2 was placed only 10 cm into the streamer chamber to allow for maximum decay length for the K^0's. Since this precluded beam measurements on the film, a separate beam-tagging system was constructed. This consisted of seven multiwire proportional chambers (MWPC). Figure 1 shows a schematic view (not to scale) of the triggering system. One of the proportional chambers PC_p, was placed directly in front of the momentum collimator with the sense wires positioned vertically to determine the beam momentum. The other six, in three groups of two chambers each, were placed between the streamer chamber and the last beam-line element. Each of the first two groups (PC_x PC_y, $PC_{x'}$ $PC_{y'}$) provided the horizontal and vertical coordinates of a beam particle, while the third ($PC_u PC_v$) had the sense wires at a 45° angle with respect to the horizontal plane. The sense wires, made of gold-plated tungsten 20 μm in diameter, had a 2-mm spacing between them. The distance between the pairs $PC_x PC_y$ and $PC_{x'}$ $PC_{y'}$ was ~1 m. The angular resolution of the system was thus ~1 mrad. The momentum resolution from chamber PC_p was limited to 30 MeV/c by the finite size of the production target PT. In addition to PC_p, a scintillation-counter hodoscope, H, consisting of nine 0.125×1.50 ×0.125-in. counters provided redundancy for the momentum determination.

The triggering system was designed to detect a "double-vee" topology following an all-neutral final state. It consisted of three distinct parts: the detection of a beam particle incident on the LH_2 target, the production of an all-neutral final state, and the detection of the strange-particle decays.

The B counters (see Fig. 1) are beam-defining counters which were comparable in size to the cross-sectional area of the beam at their locations. The A counters are anticoincidence counters. The nine strip counters of the momentum hodoscope H were logically fanned together to form a signal called H, and the beam signal was then defined to be

$$B = H \cdot B_0 \cdot B_1 \cdot B_2 \cdot B_3 \cdot B_4 \cdot \overline{(A_1 + A_5 + A_6)}.$$

Counter B_4 was a 2×2×0.625 in. scintillator placed 0.25 in. upstream from counter A_1, a 4.75×4.75×0.25-in. anticoincidence counter with a 1.75-in. beam-defining hole as shown in Fig. 1. Counters A_5 and A_6 were large paddle counters (12×30×0.375 in.) used to eliminate beam halo. Counter A_6 had a 2-in. hole to allow the beam particles through.

The signal for a produced neutral final state T

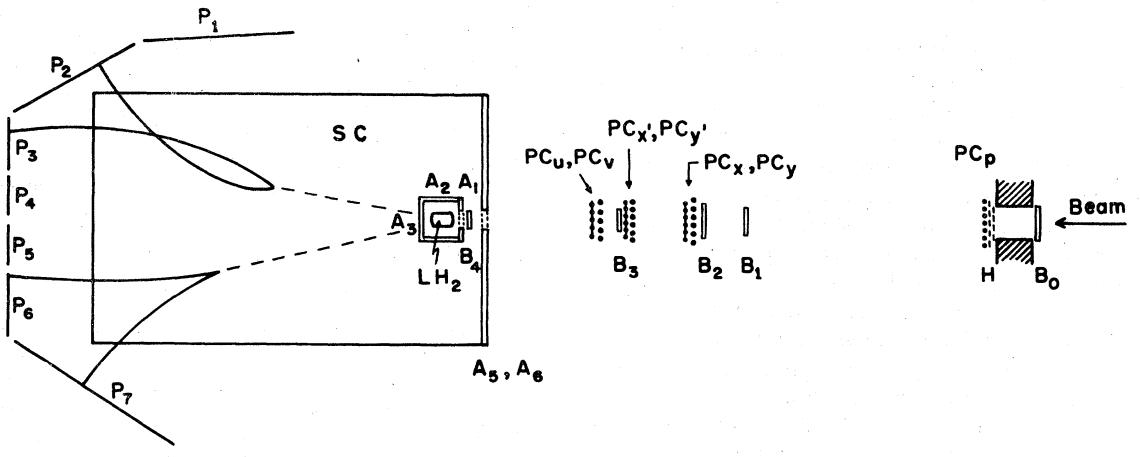

FIG. 1. Diagram of the triggering system. The trigger requirement is $B_0 \cdot H \cdot B_1 \cdot B_2 \cdot B_3 \cdot B_4 \cdot \overline{(A_2 + A_3)} \cdot \overline{(A_1 + A_5 + A_6)} \cdot (\geq 2P)$.

was defined by a beam particle into the hydrogen target and no coincidence signal from counters A_2 or A_3: $T=B\cdot(\overline{A_2+A_3})$. Counter A_3 was a 4.75 ×4.75×0.375-in. NE110 plastic scintillator located approximately 1 in. downstream from the LH_2 target. Its light was viewed by an RCA 8850 photomultiplier tube through adiabatic light pipes. Counter A_2 was a U-shaped counter 0.375 in. thick following the contour of the target foam vacuum jacket. Adiabatic light pipes from both ends of the U converged to a single RCA 8850 photomultiplier tube. Special care was taken in the design and construction of these counters to reduce the background to acceptable levels. The efficiency of the A_2-A_3 veto system was measured to be better than 3 parts in 10^7 at the 90% confidence level.

The pions produced in the K_S^0 decays were detected by a scintillation-counter hodoscope P also shown in Fig. 1. This hodoscope consisted of seven large counters, 0.125 in. thick×24 in. wide, placed around the streamer chamber as indicated in the figure. The length of these counters was optimized by Monte Carlo studies so that a maximum number of events would give signals from at least two counters. These lengths were 76.2, 47, 43, 25, 25, and 58 cm for $P1$ through $P7$, respectively. All counters were viewed through adiabatic light pipes by RCA 8575 photomultiplier tubes. The discriminated signals from all P counters were properly attenuated and then sent to a linear fan-in unit. The threshold of this unit was set so that it would provide an output only when two or more counters had coincident signals.

The event-recording process would then be initiated when the following logic was satisfied:

$$T_2=H\cdot B_0\cdot B_1\cdot B_2\cdot B_3\cdot B_4 \cdot(\overline{A_1+A_5+A_6})\cdot(\overline{A_2+A_3})\cdot(\geq 2P)\,.$$

In addition to the stereo photographs of the streamer chamber taken whenever a trigger occurred, additional information was recorded on magnetic tape to assist in the subsequent analysis. The recorded data included: the MWPC data with the beam information; three scalars recording various coincidence levels of the B counters designed to monitor the transport efficiency of the beam line; shunt currents of the beam-line magnets as well as the streamer-chamber magnet; latches for the P counters which contributed to a particular trigger; high-voltage pulse parameters; miscellaneous information such as roll and frame number, time and data, ZGS pulse count, and also some fixed data for monitoring the readout system.

III. DATA REDUCTION

The 400 000 photographs taken were scanned and measured in one pass using three image-plane and two film-plane measuring machines operating on-line with a Honeywell DDP-124 computer. The computer performed first-order tests on the quality of the measurements, requiring reasonable rms scatter of the measured points and reasonable fiducial measurements. It also automatically advanced the film on each machine, considerably speeding the scanning and measuring process. Table II contains a topological breakdown of the sample. The zero prongs are due mostly to charge-exchange reactions producing π^0's which decay into two γ rays. These, in turn, convert into e^+e^- pairs in the material surrounding the streamer chamber. Since this usually happened outside the camera's field, these frames appeared as blank frames with short incoming beam tracks. Under "other" are mostly multiprong events occurring downstream of the anticoincidence counter A_3 or even inside the target accompanied by a second beam track. Also included in this category are damaged frames, doubly exposed frames, etc. The rather well-defined background and the easily recognizable topology made losses from scanning inefficiency negligible. This was verified by double-scanning ten rolls (approximately 40 000 photographs). Only events with very dim tracks, due to occasional large jitter in the high-voltage pulse, are believed to have been missed. Corrections for this loss are included in the cross-section determination.

Approximately 30 000 double-vee events were measured. The spatial reconstruction and the kinematic identification of these events was done using the standard bubble-chamber programs TVGP and SQUAW. The spatial resolution of the reconstructed tracks was estimated to be 600 μm in space. A measure of the resulting momentum resolution is given by the width of the (unfitted) effective-mass distribution for vees satisfying the K^0 hypothesis. This distribution is

TABLE II. Topological breakdown of the scanned frames.

7 GeV/c		6 GeV/c	
Topology	Fraction (%)	Topology	Fraction (%)
0 prongs	60.0 ±0.2	0 prongs	62.0 ±0.2
1 vee	28.5 ±0.1	1 vee	26.4 ±0.2
2 vee	8.0 ±0.1	2 vee	7.1 ±0.1
3 vee	0.21±0.05	3 vee	0.17±0.01
4 vee	0.03±0.005	4 vee	0.02±0.005
Other	3.3 ±0.05	Other	4.3 ±0.06

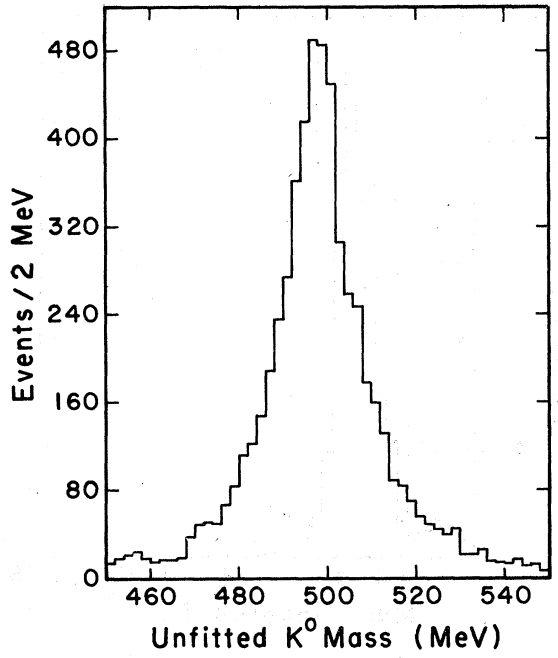

FIG. 2. Unfitted effective-mass distribution for vees consistent with the K^0 hypothesis.

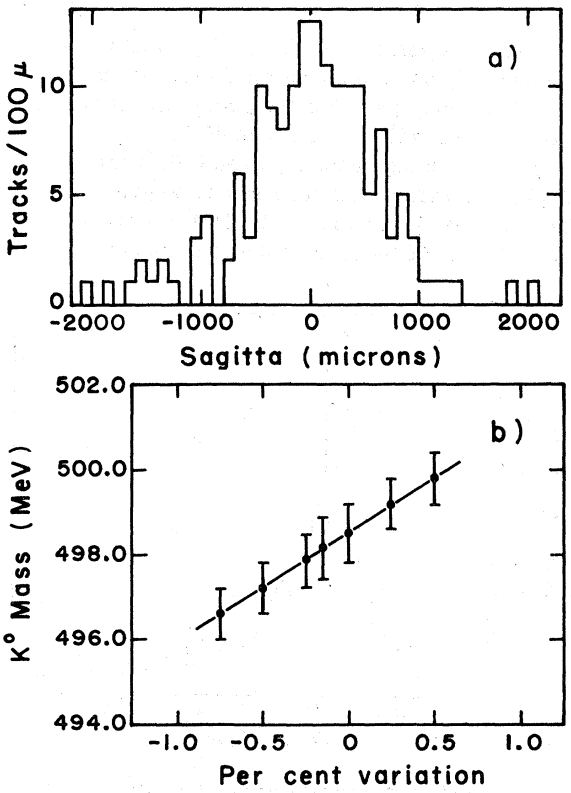

FIG. 3. (a) Distribution of the sagitta for straight tracks. (b) The unfitted K^0 effective mass as a function of the variation of the magnetic field flux.

shown in Fig. 2 and has a standard deviation of about 10 MeV.

The optical constants of the streamer chamber were determined using the program CAMADJUST. In order to test for any residual curvature in the reconstruction we used a small number of photographs which were obtained with the magnetic field turned off, triggered by two or more particles in the final state. From about 80 such events a total of 184 straight tracks were measured and processed through TVGP. One would expect the sagitta distribution for these tracks to have a width approximately equal to the average rms deviation per track, i.e., ~600 μm. Figure 3(a) shows this distribution for the 184 tracks. There are 86 "negative" and 98 "positive" tracks with 700-μm standard deviation, indicating no significant curvature. The magnitude of the magnetic field was checked by varying the flux and determining the unfitted effective mass for vees consistent with the K^0 hypothesis. Figure 3(b) shows the average mass of the K^0 determined in this way as a function of the percent variation of the magnetic flux from the value used. It can be seen that at the nominal value of the field the K^0 mass is within $\frac{1}{4}$% (Ref. 18) of the accepted value (497.7 MeV).

For over half of the measured vees the vertex was not visible or could not be accurately measured. These vertices were reconstructed by extrapolating the measured tracks using the program VERTEX.[19] The reconstruction was done in the following way. Straight lines were constructed in space at the beginning points of the decay tracks using the measured dips and azimuths of these tracks. Then a point in space was found such that the sum of the squares of the perpendicular distances to each line (appropriately weighted) was a minimum. Next the tracks were extrapolated (using helices with energy loss) to the points in space which were closest to the new vertex. (This is an iterative process which could fail to converge.) The process was then repeated and continued until the new vertex differed from the old by less than 0.05 cm. The main vertex was found by extrapolating the straight lines corresponding to the lines of flight of the two vees. It was more convenient in practice to use the center of the target as the main vertex (with errors equal to $\frac{1}{3}$ of the size of the target in the corresponding direction) and let the overall SQUAW fit determine its actual position through adjustments to the vee angles. In this way the overall error structure was more reasonable.

All the successfully reconstructed events were then processed by SQUAW. For every vee the K^0,

Λ, $\bar{\Lambda}$, and γ hypotheses were tried. For every event with both vees obtaining at least one successful three-constraint (3C) fit, the following multivertex hypotheses were then tried, depending on the nature and the number of the vee fits: ΛK^0_S, $\Lambda K^0_S \pi^0$, $n K^0_S K^0_S$, and $\Lambda \bar{\Lambda} n$. All the events which failed to obtain a 3C fit for both vees were remeasured and reprocessed. Events which failed for the second time were accounted for in the cross sections after a careful study of such events.

In order to understand the nature of the vee fits and resolve kinematic ambiguities a sample of 5048 double-vee events, representing approximately $\frac{1}{6}$ of the total sample, was studied in detail. A study of the χ^2 distributions for different event hypotheses led to the adoption of the following event selection criteria. A hypothesis was rejected if its χ^2 was greater than 15.0 (corresponding to a confidence level of 0.2% for 3 degrees of freedom). Furthermore, for the ambiguous fits, a hypothesis was chosen if its χ^2 probability was greater than 20 times the probability of any other successful hypothesis. The results, after these cuts, are summarized in Table III.

Figure 4 shows a plot of the square of the effective mass (unfitted) for unique K^0 fits calculated assuming e^+-e^- masses for the decay products. γ-ray contamination in the K^0 sample appears as a peak at ≈ 0.05 GeV^2. Thus, events with an effective mass squared (calculated as described above) less than 0.084 GeV^2 were assumed to be electron-positron pairs and were discarded.

A final sample of 5096 $n K^0_S K^0_S$ events was selected from approximately 16 000 candidates with both vees identified as K^0's. All the appropriate multivertex hypotheses were tried and an event was selected if the $n K^0_S K^0_S$ hypothesis was the only one surviving the following cuts:

(a) A fit was ignored if the event also obtained a 10C ΛK^0_S fit with χ^2 less than 45.0.

(b) The missing-mass squared (MM^2) for the $n K^0_S K^0_S$ hypothesis was required to be greater than 0.32 GeV^2. In Fig. 5 the MM^2 spectrum for a sample of these candidates is shown. The

TABLE III. Summary of results of the single-vertex fits.

		No cuts (%) [a]	χ^2 cuts (%) [a]	Probability decisions (%) [a]
Unique (76% of total)	Λ	15	17	18
	K^0	62	66	68
	$\bar{\Lambda}$	1	1	1
	γ	0.1	0.1	0.1
Ambiguous (11% of total)	Λ-K^0	16	11	9
	Λ-$\bar{\Lambda}$	0.1	0.1	0.1
	$\bar{\Lambda}$-K^0	6	4	3.9
	3 fits	0.2	0.1	...
No fits (13% of total)		...	...	...

[a] Percent fraction of fitted vees.

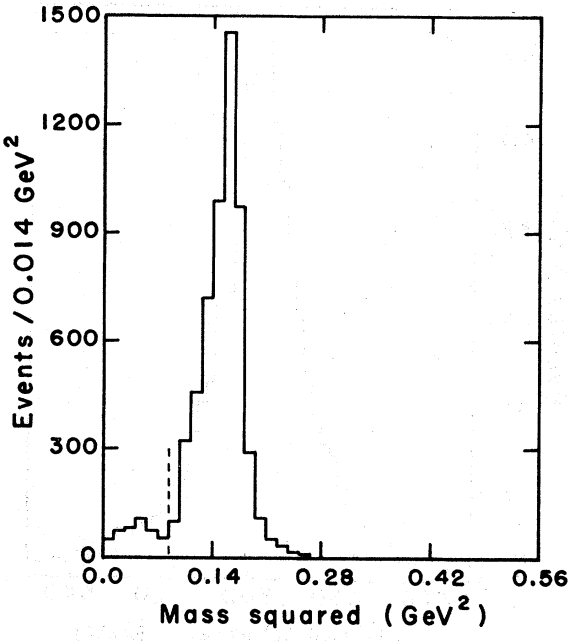

FIG. 4. Unfitted effective-mass-squared distribution for vees consistent with the K^0 hypothesis and the vee decay products assuming e^+e^- masses. The broken line represents the cut at 0.084 (GeV)^2 to eliminate γ contamination.

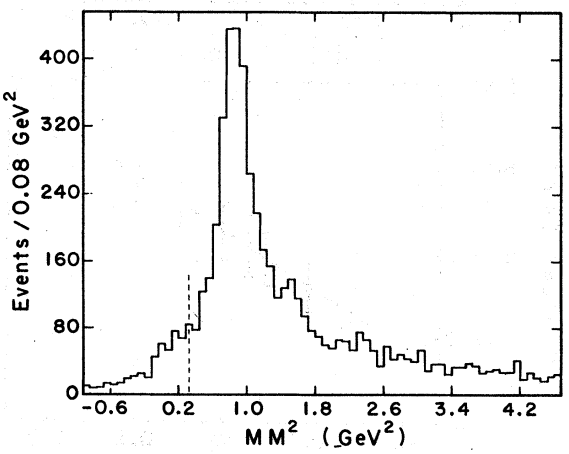

FIG. 5. Missing-mass-squared distribution for events with both vees consistent with the K^0 hypothesis. The broken line represents the missing-mass cut for the $n K^0_S K^0_S$ selection.

broken line indicates the cut described above.

(c) The MM^2 for the $\Lambda K^0_S \pi^0$ hypothesis was required to satisfy $-0.08 < MM^2 < 0.12$ GeV^2 in order to be an acceptable fit. These limits correspond to the values $m_\pi{}^2 \pm 3m_\pi{}^2$, where $m_\pi{}^2$ is the square of the mass of the π^0.

(d) The χ^2 cut, $\chi^2 < 20.0$, for the $nK^0_S K^0_S$ hypothesis was imposed on the basis of Fig. 6 which shows MM^2 plotted against the χ^2 of the fit. This distribution is expected to be symmetric with respect to the horizontal line corresponding to the mass squared of the neutron. It can be seen, however, that the high-mass tail is more heavily populated for large values of χ^2. This indicates some contamination from $nK^0_S K^0_S \pi^0$ events. The cut shown by the broken line eliminates only a few good events and most of the ones with an additional π^0.

(e) Events were rejected if the square of the four-momentum transfer at the nucleon vertex was greater than 2 $(\mathrm{GeV}/c)^2$. This cut was imposed because it was found that the statistical weights for such events were very high (>8.0). In the total sample there were only 34 such events.

(f) Finally, fiducial-volume cuts were imposed on the decay vertex of the vees. One might ordinarily expect to impose an additional cut on the main vertex position so as to restrict the interaction to occur in the liquid hydrogen. It was found that in this experiment such a cut would considerably bias the $K^0_S K^0_S$ sample, particularly in the low-effective-mass region. This is because the primary event vertex cannot be seen and is determined by extrapolating the momenta of the strange particles. Such an extrapolation is inaccurate when the opening angle is small (i.e., less than ~12°). This angle is smaller for lower $K^0_S K^0_S$ masses because of the lower Q value available to the K^0's and, therefore, the uncertainty in the determination of the x coordinate of the vertex for this mass region is higher. Vertex position cuts would, thus, result in a relative loss of low-mass events, intensified by the short length of the liquid-hydrogen target (7.5 cm). In Fig. 7 histograms of the x coordinate of the main vertex are shown for (a) "target-full" and (b) "target-empty" samples. The two peaks in the target-empty histogram correspond to events in the PVC foam used for thermal insulation. The decision to include the events originating in the PVC foam (estimated to be about $\frac{1}{4}$ of the total sample) was made after carefully studying a sample of about 20 000 target-empty photographs taken during an early run. None of the appropriate distributions for events fitting $nK^0_S K^0_S$ showed any noticeable differences from the corresponding ones from the hydrogen events.

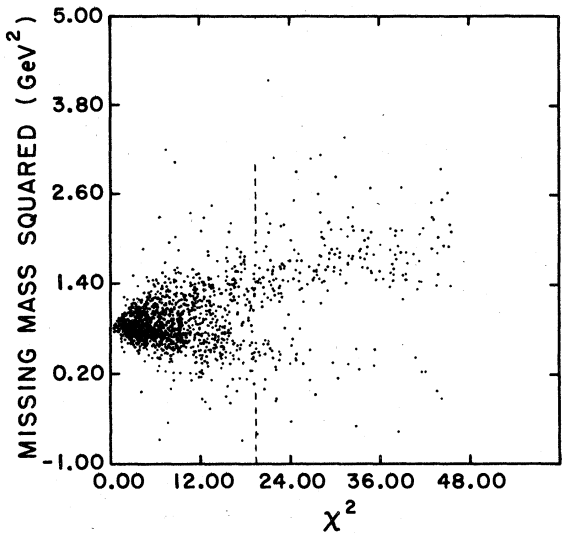

FIG. 6. Missing-mass squared for the 7C $n K^0_S K^0_S$ fits as a function of the χ^2 of the fit. The broken line indicates the applied cut for the $n K^0_S K^0_S$ selection.

Table IV shows the number of events fitting the various hypotheses after all the cuts described above. The contamination of the $nK^0_S K^0_S$ sample due to events with one or more π^0's is estimated to be ~8% from the asymmetry of the MM^2 distribution (not shown) for fitted $nK^0_S K^0_S$ events.

For every event detected, a number of events with the same dynamical characteristics may be produced, but escape detection because of the limited solid angle subtended by the scintillation counter hodoscope, the position and sizes of the

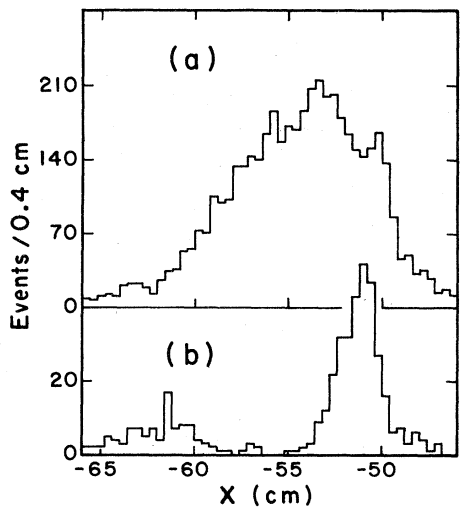

FIG. 7. Distribution of the x coordinate (along the beam) of the primary vertex for (a) target-full and (b) target-empty samples.

TABLE IV. Results of the multivertex fits. All numbers presented include data from 6 and 7 GeV/c. Possible γ contamination in the Λ, $\bar{\Lambda}$ samples not subtracted.

	Channel	Number of events	Channel	Number of events
Unique	$nK_S^0K_S^0$	5096	$K_S^0K_S^0+X^0$	7303
	ΛK	534	$\Lambda K+X^0$	6850
	$\Lambda K\pi^0$	1701	$\Lambda\bar{\Lambda}+X^0$	683
	$\Lambda\bar{\Lambda}n$	321		
Ambiguous	$nK_S^0K_S^0$-$\Lambda K\pi^0$	34	$K_S^0K_S^0$-ΛK^0	785
	nK^0K^0-$\Lambda\bar{\Lambda}n$	2	$K_S^0K_S^0$-$\Lambda\bar{\Lambda}$	20

various counters of the triggering system, and other geometrical factors. The following Monte Carlo method was used to determine the detection probability for each $nK_S^0K_S^0$ event. The parameters dynamically defining an event are: the square of the total center-of-mass energy, s; the square of the four-momentum transfer at the nucleon vertex, t; the $K_S^0K_S^0$ effective mass, M_{KK}; and the $K_S^0K_S^0$ decay angles θ_J, ϕ_{TY} defined in the Jackson-Gottfried reference frame. For each detected event these parameters were calculated and then the following parameters were generated randomly: the x coordinate of the main vertex, x; the proper lifetimes[20] of the two K^0's, τ_1 and τ_2; the overall azimuthal angle in the c.m. system, ϕ; and $\cos\theta_\pi$ and ϕ_π defined as the cosine of the polar angle and the azimuthal angle of the positive pion in the K^0's rest frame for each of the two K^0's. With these parameters an event was generated and was examined to determine whether it would have triggered the streamer chamber. The process was stopped when 100 triggers were counted. The weight would then be equal to $N/100$, where N is the total number of generated events. It was found that the weights vary smoothly as a function of the $K_S^0K_S^0$ mass, $|t|$ and $\cos\theta_J$. The average weight is 2.05 at 7.0 GeV/c and 2.25 at 6.0 GeV/c. This corresponds to an overall average detection probability of 48%.

IV. CROSS SECTION FOR THE REACTION $\pi\bar{p} \to nK_s^0K_s^0$

We calculated the raw cross section for reaction 1 using the equation

$$\sigma = \frac{NA}{\rho L N_0},$$

where N is the number of events observed in a given sample, L the total beam length in hydrogen, ρ and A the density and atomic weight of hydrogen, and N_0 Avogadro's number. The total beam track length was corrected for nonpion beam contamination, losses due to δ rays produced in the target, losses from neutron scatters, and the light loss due to incorrect beam vetoes[21] as described in Ref. 1. In that reference, we reported the cross section for the reaction $\pi^- p \to$ (all neutrals) in this experiment. The results of that measurement yielded results quite consistent with other measurements in the literature.

We determined the number of events produced in the liquid hydrogen using the primary vertex coordinate histograms in Fig. 7 by subtracting the target-empty distribution from the target-full after properly normalizing the first so that the two peaks representing the downstream PVC foam coincide. It was thus estimated that 74% ± 10% of the events originated in the liquid hydrogen. The raw cross sections calculated for both incident momenta were multiplied by this factor to obtain the corresponding cross sections for hydrogen.

A further correction factor 1.05 ± 0.05 was used to compensate for the $nK_S^0K_S^0$ events among those which failed to obtain 3C fits for both vees after two measurements. A more accurate estimate is hampered by the small energy loss in the streamer chamber making identification of electrons particularly difficult.

Finally, a factor of 2.115 was used to account for the neutral decay mode of the K_S^0. This factor is obtained from the inverse of the probability that either or both K_S^0's decay into two neutral pions.

The raw cross sections for both incident momenta, the corrections above and other appropriate corrections, as well as the final cross sections are presented in Table V. The total number of the unweighted events and the observable part of the cross section determine the sensitivity of this experiment to be 1.1 events/nb.

TABLE V. Corrections and the cross sections for the $nK_S^0K_S^0$ state.

Incident momentum (GeV/c)	6.0	7.0
Raw cross section: $NA/\rho LN_0$ (μb) [a]	2.42 ±0.17	2.14 ±0.14
Non-hydrogen events $=F_1$	0.74 ±0.07	0.74 ±0.07
No-fits $=F_2$	1.05 ±0.05	1.05 ±0.05
Neutral decay mode $=F_3$	2.115	2.115
Average weight $=F_4$	2.25	2.02
Streamer chamber insensitive $=F_5$	1.068 ±0.006	1.101 ±0.006
Inefficiency of scintillation counters $=F_6$	$(1.03 \pm 0.02)^2$	$(1.03 \pm 0.02)^2$
Missing mass, χ^2 cuts $=F_7$	0.95 ±0.02	1.05 ±0.02
$\sigma(\pi^- p \to nK_S^0K_S^0)$ (μb) [b]	9.64 ±1.27	8.69 ±1.13

[a] Calculated with corrected beam track length.
[b] $\sigma = \sigma_{\text{raw}} F_1 F_2 F_3 F_4 F_5 F_6 F_7$.

V. ANALYSIS OF THE $nK_S^0K_S^0$ FINAL STATE

A. General characteristics

One of the striking features of the $K_S^0K_S^0$ system evident even in the early low-statistics experiments was the rich structure in the effective-mass spectrum. This is shown in Fig. 8 for the 5096 events of this experiment. The shaded histogram represents the raw data, whereas the full histogram represents the data corrected for geometrical acceptance as discussed in Sec. III. The smooth variation of the average weights as a function of mass can be noted, with average weights a little less than 2 near threshold and a little over 2.5 at 2000 MeV. The average effective-mass resolution is quite good near threshold and less than 15 MeV for most of the data. The prominent threshold enhancement shows a sudden rise at threshold and a statistically significant dip at ≈1150 MeV. The prominent peak around 1350 MeV is primarily due to f production although A_2^0 and f' are known to contribute. The enhancement at 1440 MeV reported by Beusch *et al.*[8] can also be seen. The mass spectra for the 6.0- and 7.0-GeV/c data separately (not shown) show, within statistics, similar behavior.

In Fig. 9 the scatter plot of the K_S^0n effective mass versus the $K_S^0K_S^0$ effective mass is shown. Again the threshold enhancement and the structure around 1350 MeV are evident. It is clear from this figure that the observed enhancements are not reflections from Y^* production since no structure can be seen in the K_S^0 system.

The distribution of the square of the four-momentum transfer, t, for all events is shown in Fig. 10. Again, the smooth variation of the acceptance as a function of t is obvious. A Chew-Low plot for the data is shown in Fig. 11. The peripheral production of the $K_S^0K_S^0$ system is evident with the majority of the events produced with $-t<0.2$ (GeV/c)^2. A narrow band extending to higher $|t|$, however, can be seen around 1300 MeV suggesting some production mechanism different from the rest of the data.

The decay angular distributions for the $K_S^0K_S^0$ system in the t channel (Gottfried-Jackson

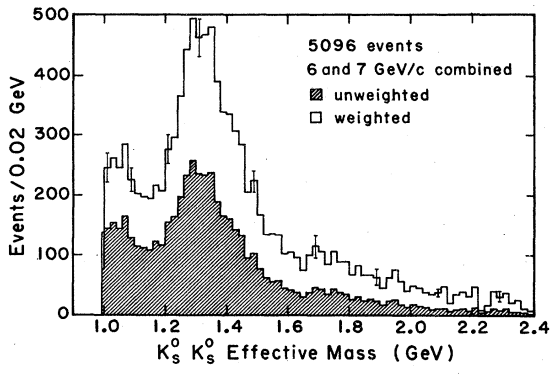

FIG. 8. The $K_S^0K_S^0$ effective-mass spectrum.

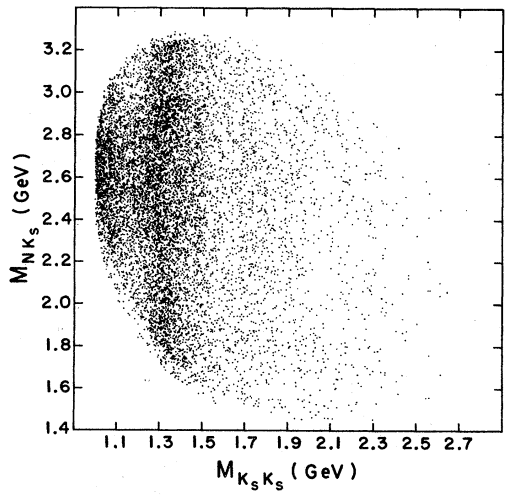

FIG. 9. Effective mass of the nK_S^0 versus the effective mass of the $K_S^0K_S^0$.

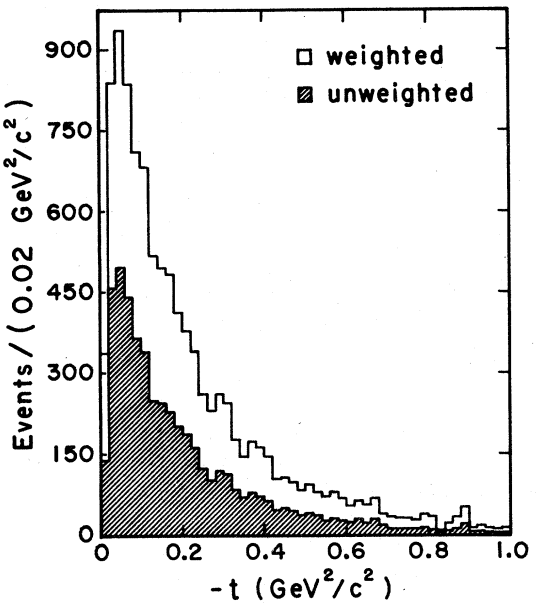

FIG. 10. Distribution of the four-momentum transfer squared at the nucleon vertex.

frame) are shown in Figs. 12 and 13 in 100-MeV effective-mass bins. Both distributions are folded because the two K_S^0's are indistinguishable. The acceptance varies slowly as a function of the cosine of the polar angle (Jackson angle) becoming smaller as $\cos\theta_J$ approaches 1. As a function of mass, the $\cos\theta_J$ distribution is nearly isotropic at threshold, indicating dominance of $K\bar{K}$ production with angular momentum $l=0$. The contribution of $l=2$ states becomes important in the f-A_2-f' region, diminishing again at higher masses. The distributions of the azimuthal angle (Treiman-Yang angle) are quite consistent with isotropy even at higher masses when the statistics become rather poor. Treiman and Yang have shown[22] that this is a necessary but not a sufficient condition for $K\bar{K}$ production via a one-pion-exchange mechanism. We parametrized the angular distributions in terms of the moments of the spherical harmonics:

$$\frac{d^4\sigma}{dt\,dM\,d\Omega} = N \sum_{l=0}^{l_{\max}} \left(\langle Y_l^0 \rangle Y_l^0(\Omega) + 2 \sum_{m=1}^{m_{\max}} \langle \mathrm{Re} Y_l^m \rangle \mathrm{Re} Y_l^m(\Omega) \right), \quad (2)$$

where $d\Omega$ is the element of angular space in the Gottfried-Jackson frame; $N \propto d^2\sigma/dMdt$ is the number of events observed in a given M and t bin (M is the $K_S^0 K_S^0$ effective mass and t is the square of the four-momentum transfer from the target proton to the outgoing neutron); and the $Y_l^m(\Omega)$ are the normalized spherical harmonics. The coefficients $\langle Y_l^m \rangle$ of the expansion are proportional to the expectation values, i.e., the moments of the spherical harmonics. In the case of the $K_S^0 K_S^0$ system, the fact that the two K_S^0's are indistinguishable implies that only terms with even l contribute. Furthermore, from parity conservation, only $\mathrm{Re} Y_l^m$ for $m \neq 0$ are nonvanishing. Then the moments of the spherical harmonics are given by

$$\langle \mathrm{Re} Y_l^m \rangle = \int \frac{d^4\sigma}{dMdtd\Omega} \mathrm{Re} Y_l^m(\Omega) d\Omega \Big/ \int \frac{d^4\sigma}{dMdtd\Omega} d\Omega . \quad (3)$$

We have used the maximum-likelihood method to determine these moments. The combined 6.0- and 7.0-GeV/c data were divided in two t bins $|t_{\min}| \leq |t| \leq 0.2$ (GeV/c)^2 and $0.2 \leq |t| \leq 0.5$ (GeV/c)^2 and 15 mass bins (twelve 50-MeV bins from threshold to 1600 MeV and three 100-MeV bins from 1600 to 1900 MeV). The results for the low-t bin are shown in Fig. 14, where the unnormalized t-channel moments are shown as a function of the $K\bar{K}$ mass. Spherical harmonics with $l \geq 6$ as well as the ones with $l = 4$ and $m = 3, 4$ were also included, but their moments were found to be consistent with zero.

The goodness of the maximum-likelihood fits was tested using the following χ^2 method. For each (M, t) bin the angular space was divided in a 5×3 grid in $\cos\theta_J$ and ϕ_{TY}, respectively. Predictions for the population of these bins were then generated using the best parameters from

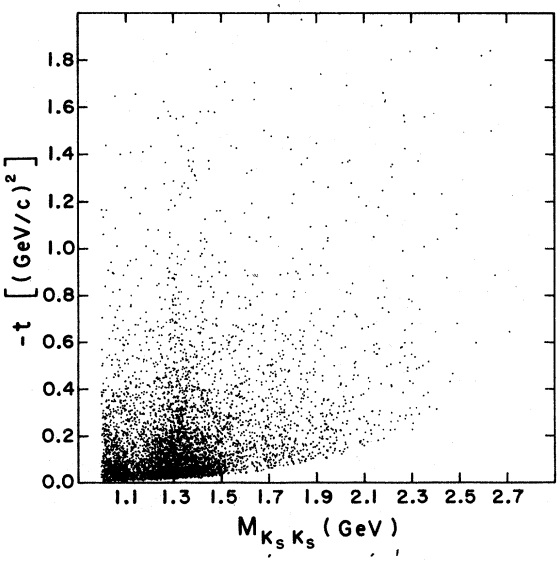

FIG. 11. Scatter plot of $|t|$ versus the $K_S^0 K_S^0$ effective mass.

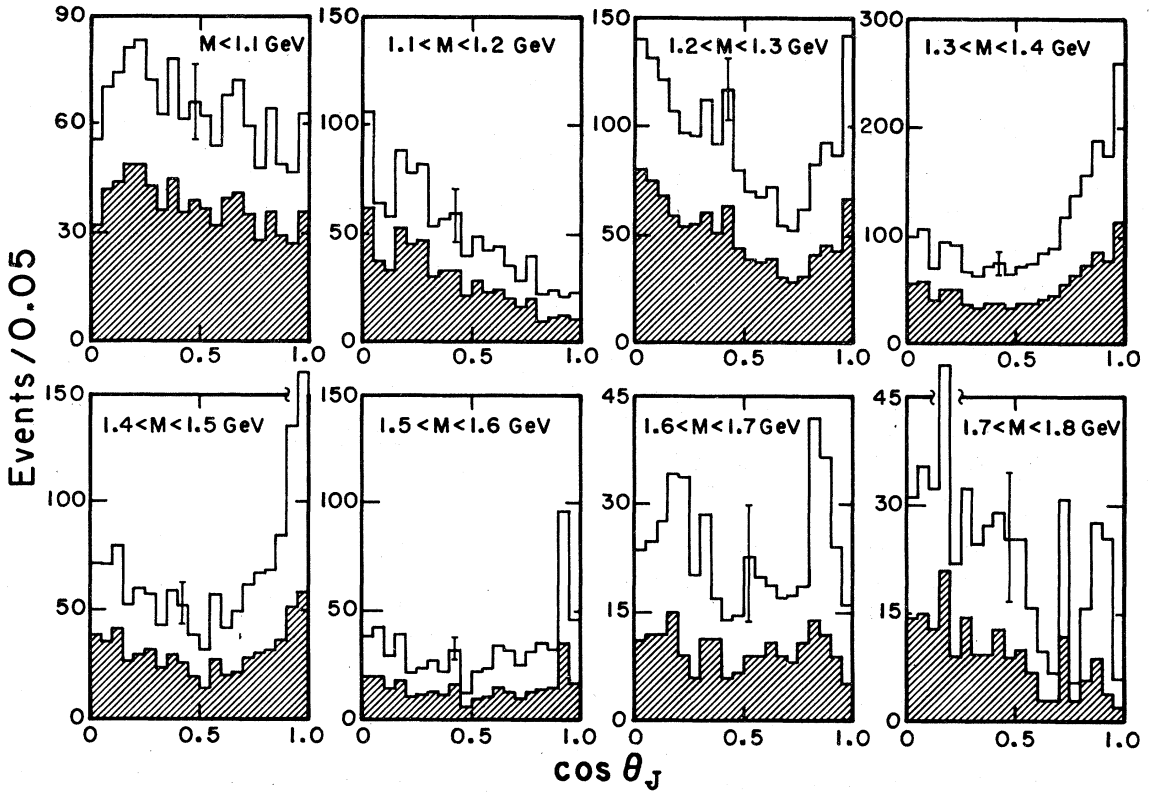

FIG. 12. The weighted and unweighted (shaded) $\cos\theta_J$ distributions as a function of $K_S^0 K_S^0$ effective mass.

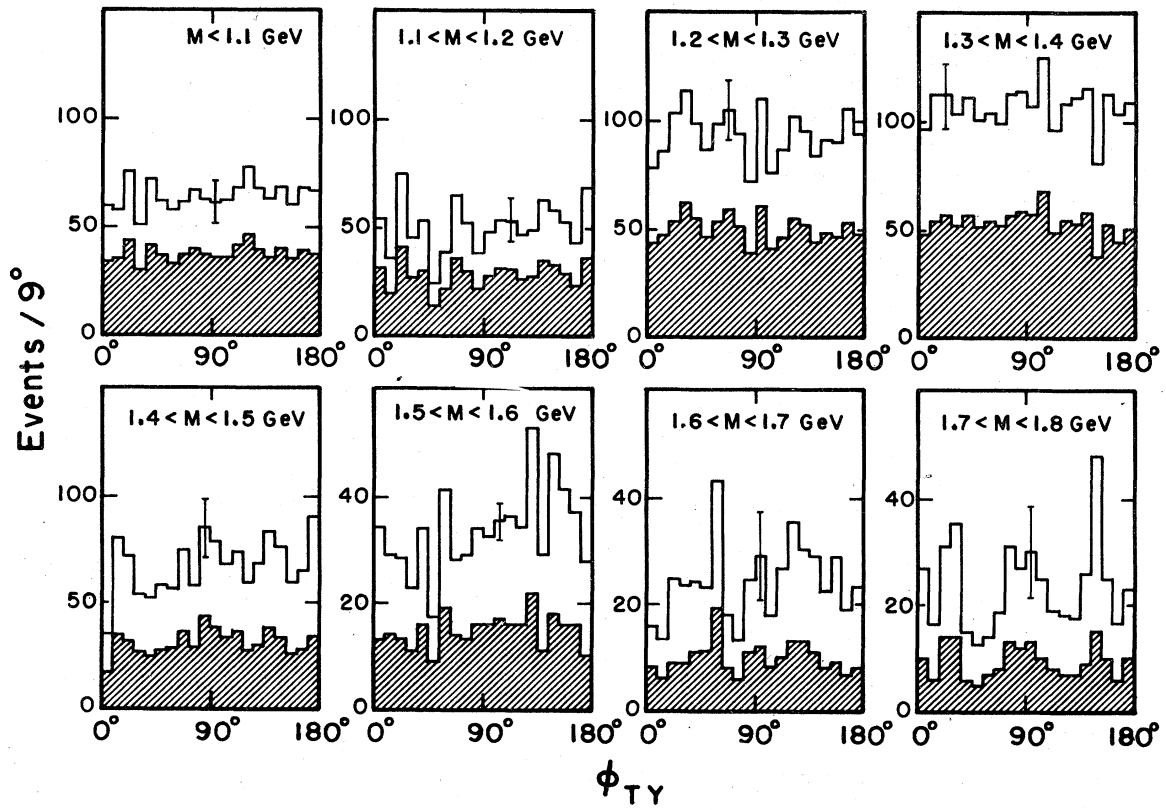

FIG. 13. The weighted and unweighted (shaded) Treiman-Yang angle distribution as a function of $K_S^0 K_S^0$ effective mass.

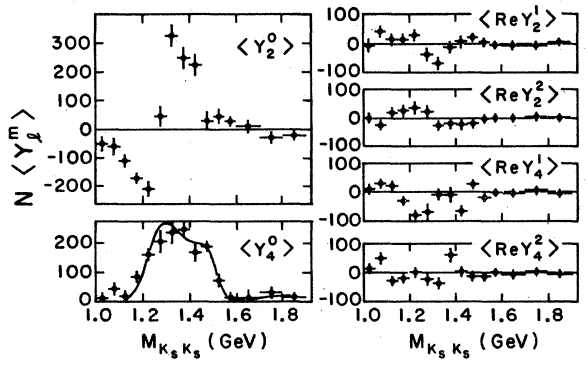

FIG. 14. Unnormalized t-channel moments $\langle \mathrm{Re}\, Y_l^m \rangle$ as a function of the $K_S^0 K_S^0$ effective mass for $|t| < 0.2$ (GeV/c)^2. The solid line represents the f-f' fit to the data as described in the text.

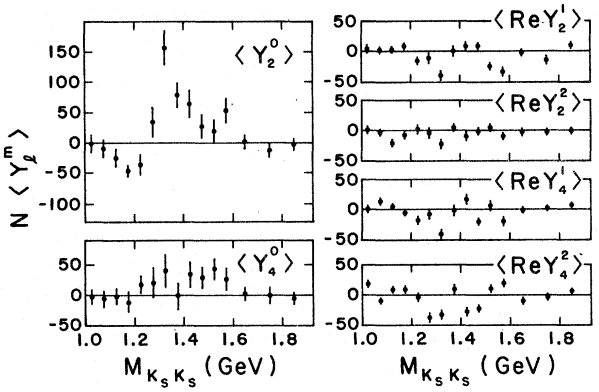

FIG. 15. Unnormalized t-channel moments $\langle \mathrm{Re}\, Y_l^m \rangle$ as a function of the $K_S^0 K_S^0$ effective mass for $0.2 < |t| < 0.5$ (GeV/c)^2.

the likelihood fit, a^*, and values for the spherical harmonics, $\overline{Y}_k$, averaged over a given bin. Then a χ^2 was computed as follows:

$$\chi^2 = \sum_{i=1}^{15} \left(\frac{N_w}{15} \sum_{k=1}^{k_{\max}} a_k^* \overline{Y}_k - \sum_{j=1}^{N_i} w_j \right)^2 \Big/ \sum_{j=1}^{N_i} w_j^2 , \qquad (4)$$

where N_w is the total number of weighted events in the (M, t) bin and N_i is the weighted number of events in the ith $(\cos\theta_X, \phi_{TY})$ bin. The χ^2's obtained in this way were acceptable, varying from 5.0 to 20.0 for 8 degrees of freedom. The results for the $t_{\min} < |t| < 0.2$ (GeV/c)^2 bin as a function of mass are shown in Table VI.

Qualitatively, the results of the moments analysis shown in Fig. 14 for the low-t bin can be described as follows.

(a) The $K_S^0 K_S^0$ system is produced predominantly in helicity-zero states in the t channel. Some production in helicity-one states, however, is also present, as indicated by the nonzero values of the $m = 1$ and $m = 2$ moments.

(b) Since the $\langle Y_2^0 \rangle$ moment contains contributions from D-wave states as well as an S- and D-wave interference term, and since the D-wave contribution is positive definite, the large negative excursion below 1300 MeV indicates the presence of a relatively strong S-wave coherent with the D wave in that region. It is worth noticing that $\langle Y_2^0 \rangle = 0$ approximately at the mass of the f meson.

(c) The $\langle Y_4^0 \rangle$ moment, which results exclusively from D-wave contributions, shows a broad enhancement centered about 1300 MeV. At $|t| < 0.2$ (GeV/c)^2 A_2 production is expected to be

TABLE VI. Moments of the angular distributions for $|t| < 0.2$ (GeV/c)^2. These are unnormalized t-channel moments presented as $\sqrt{4\pi} N \langle \mathrm{Re}\, Y_l^m \rangle$ (events/0.05 GeV).

Mass bin (GeV)	$\langle Y_0^0 \rangle$	$\langle Y_2^0 \rangle$	$\langle \mathrm{Re}Y_2^1 \rangle$	$\langle \mathrm{Re}Y_2^2 \rangle$	$\langle Y_4^0 \rangle$	$\langle \mathrm{Re}Y_4^1 \rangle$	$\langle \mathrm{Re}Y_4^2 \rangle$	χ^2 [a]
Thresh–1.05	472.4 ± 28	−50.9 ± 28	−1.3 ± 10	1.5 ± 11	8.1 ± 27	12.2 ± 11	11.1 ± 11	15.4
1.05–1.10	454.4 ± 28	−61.1 ± 28	41.9 ± 9	−54.0 ± 11	44.0 ± 28	31.3 ± 9	48.3 ± 9	13.4
1.10–1.15	323.4 ± 24	−111.1 ± 20	8.6 ± 7	20.7 ± 10	19.2 ± 20	20.7 ± 7	−30.3 ± 8	10.1
1.15–1.20	380.4 ± 26	−174.4 ± 21	11.9 ± 7	28.5 ± 10	92.7 ± 22	−31.5 ± 8	−19.9 ± 7	7.9
1.20–1.25	565.6 ± 32	−206.6 ± 30	33.6 ± 9	34.5 ± 13	166.1 ± 28	−83.1 ± 10	0.0 ± 10	13.4
1.25–1.30	740.7 ± 37	46.6 ± 42	−39.5 ± 12	20.8 ± 13	211.8 ± 38	−81.0 ± 14	−23.2 ± 13	7.1
1.30–1.35	718.8 ± 38	326.3 ± 45	−65.2 ± 12	−31.2 ± 11	240.3 ± 41	−3.4 ± 14	−37.0 ± 13	18.5
1.35–1.40	653.9 ± 37	249.8 ± 43	−16.8 ± 13	−27.0 ± 11	250.3 ± 38	−5.1 ± 14	65.9 ± 12	6.2
1.40–1.45	525.4 ± 33	226.6 ± 40	5.8 ± 11	−26.3 ± 10	174.0 ± 36	−62.4 ± 12	3.3 ± 11	15.9
1.45–1.50	338.8 ± 27	29.6 ± 33	21.2 ± 7	−24.8 ± 9	188.4 ± 22	37.1 ± 11	−9.5 ± 9	11.1
1.50–1.55	195.3 ± 21	48.8 ± 26	0.9 ± 7	−5.3 ± 7	77.5 ± 24	−20.1 ± 8	−10.4 ± 7	17.2
1.55–1.60	125.3 ± 17	2.9 ± 19	−6.5 ± 6	−2.7 ± 6	10.6 ± 18	0.6 ± 7	−1.9 ± 7	13.5
1.60–1.70	55.4 ± 6	4.8 ± 7	−5.1 ± 2	−0.7 ± 2	7.2 ± 8	−4.4 ± 2	−3.7 ± 2	18.2
1.70–1.80	49.2 ± 6	−18.0 ± 6	−5.4 ± 2	1.2 ± 2	16.7 ± 6	3.7 ± 2	4.2 ± 2	9.9
1.80–1.90	26.3 ± 4	−11.0 ± 4	3.4 ± 2	0.9 ± 2	7 ± 5	−4.1 ± 1	−1.3 ± 2	5.9

[a] For 8 degrees of freedom.

TABLE VII. Moments of the angular distributions for $0.2 \leq |t| \leq 0.5\,(\mathrm{GeV}/c)^2$. These are unnormalized t-channel moments presented as $\sqrt{4\pi}\,N\,\langle \mathrm{Re}\,Y_l^m \rangle$ (events/0.05 GeV).

Mass bin (GeV)	$\langle Y_0^0 \rangle$	$\langle Y_2^0 \rangle$	$\langle \mathrm{Re}\,Y_2^1 \rangle$	$\langle \mathrm{Re}\,Y_2^2 \rangle$	$\langle Y_4^0 \rangle$	$\mathrm{Re}\,\langle Y_4^1 \rangle$	$\mathrm{Re}\,\langle Y_4^2 \rangle$	$\chi^{2\,a}$
Thresh–1.05	147.5 ± 16	−0.9 ± 16	5.1 ± 6	1.6 ± 6	−3.2 ± 14	1.6 ± 6	17.3 ± 5	8.7
1.05–1.10	126.9 ± 15	−7.9 ± 14	3.2 ± 5	−3.2 ± 5	−6.3 ± 14	12.7 ± 5	−9.5 ± 5	44.3
1.10–1.15	128.6 ± 15	−24.1 ± 15	4.4 ± 5	−19.7 ± 5	−2.0 ± 13	4.0 ± 5	8.0 ± 5	7.0
1.15–1.20	101.7 ± 14	−46.1 ± 9	8.0 ± 5	−6.0 ± 6	−11.8 ± 17	−5.2 ± 3	7.6 ± 5	16.3
1.20–1.25	157.5 ± 17	−35.4 ± 16	−16.4 ± 5	3.3 ± 7	18.2 ± 15	−18.0 ± 6	−5.2 ± 6	16.1
1.25–1.30	258.6 ± 22	34.7 ± 24	−11.3 ± 7	−4.4 ± 8	20.2 ± 24	−8.1 ± 8	−37.2 ± 8	26.5
1.30–1.35	328.0 ± 26	156.8 ± 28	−39.5 ± 9	−21.7 ± 7	37.9 ± 27	−41.5 ± 9	−32.8 ± 8	7.7
1.35–1.40	222.8 ± 21	80.1 ± 22	1.9 ± 9	4.5 ± 6	−2.8 ± 22	−1.6 ± 8	9.1 ± 8	44.7
1.40–1.45	192.7 ± 20	65.1 ± 23	8.4 ± 7	−9.0 ± 6	33.7 ± 21	16.9 ± 8	−27.7 ± 7	7.9
1.45–1.50	129.5 ± 17	28.3 ± 19	8.8 ± 5	−1.2 ± 5	28.9 ± 18	−19.8 ± 5	−23.2 ± 5	10.7
1.50–1.55	135.8 ± 18	19.5 ± 21	−23.5 ± 6	5.1 ± 6	42.4 ± 17	6.2 ± 7	9.7 ± 6	19.8
1.55–1.60	115.2 ± 17	53.9 ± 20	−34.4 ± 6	−9.1 ± 5	26.9 ± 17	−20.0 ± 7	18.8 ± 6	10.2
1.60–1.70	85.2 ± 10	1.6 ± 11	−1.6 ± 4	−2.5 ± 4	1.9 ± 11	−1.9 ± 4	−10.5 ± 4	12.3
1.70–1.80	91.5 ± 11	−11.1 ± 11	−12.1 ± 4	−1.8 ± 4	−0.6 ± 12	1.7 ± 4	−3.1 ± 4	5.5
1.80–1.90	68.9 ± 10	−1.0 ± 10	9.8 ± 4	−0.2 ± 4	−4.5 ± 9	7.5 ± 4	6.2 ± 4	4.5

[a] For 8 degrees of freedom.

very small.[9] The same is true for f' production via one-pion exchange since coupling of the f' to two pions is forbidden by the Okubo-Zweig-Iizuka rule[23,24]. However, it is obvious that the data are inconsistent with only f production.

The moments of the angular distributions for the $0.2 < |t| < 0.5\ (\mathrm{GeV}/c)^2$ bin are shown in Fig. 15 and are given in Table VII. They show the same general characteristics although the f production is markedly suppressed as would be expected for f production via π exchange. There is again a clear indication of S-D interference in the 1200–1400-MeV mass region.

B. D-wave parametrization

It was already mentioned in the previous section that simple f-meson production cannot explain the observed enhancement in the $\langle Y_4^0 \rangle$ moment. Furthermore, f^0-A_2^0 interference can be ruled out as the cause of the enhancement using the following argument. It has been pointed out[25] that the interference term between an $I=0$ and an $I=1$ resonance will have an overall phase difference of 180° in the reaction $\pi^- p \to n K_S^0 K_S^0$ relative to the production in the reaction $\pi^- p \to n K^+ K^-$. One expects markedly different shapes in $\langle Y_4^0 \rangle$ in the two reactions if, for example, f^0-A_2^0 interference is large. However, the $\langle Y_4^0 \rangle$ observed in the K^+K^- data[26] is quite similar to our data, and we must exclude f-A_2 interference alone as the explanation for the observed enhancement.

The amount of A_2 expected in our data can be deduced from cross-section measurements as a function of t in the literature.[27,28] Figure 16 shows the distribution in M for $|t| < 0.2$ $(\mathrm{GeV}/c)^2$ and for $0.2 \leq |t| \leq 0.5$ $(\mathrm{GeV}/c)^2$ along with the predicted A_2 signal. It is clear that A_2 production is relatively small, especially in the low $|t|$ range where the following analysis is carried out.

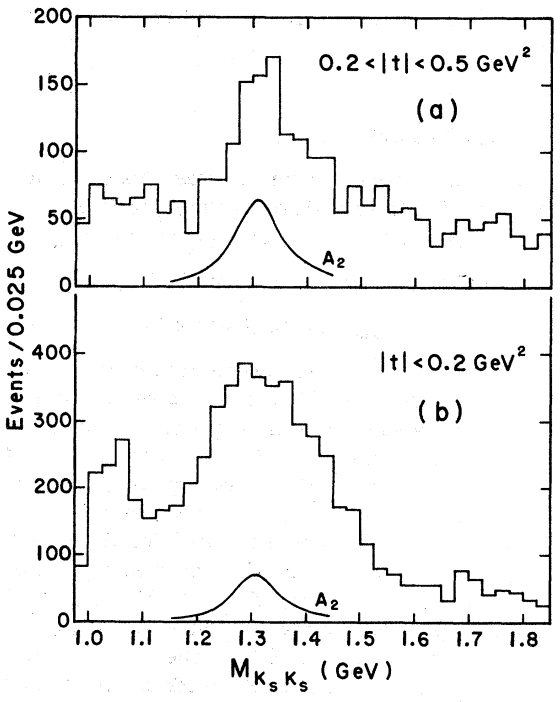

FIG. 16. Distribution of the $K_S^0 K_S^0$ effective mass for (a) $0.2 \leq |t| \leq 0.5$ $(\mathrm{GeV}/c)^2$ and for (b) $|t| < 0.2$ $(\mathrm{GeV}/c)^2$. The smooth curves shown are the expected A_2^0 contributions calculated as described in the text.

[Pawlicki *et al.*[29] have determined that a small amount of A_2^0 is present and interferes with both f and f' production amplitudes. The f-A_2^0 interference is only significant for $|t| > 0.2$ (GeV/c)^2.]

The similarity between the Y_4^0 moments observed in our data and in the data of Pawlicki *et al.*[26] would be understandable if the interfering amplitudes were not different I spin but of the same,[29] i.e., were due to f interfering with f'. The D wave (or equivalently the $\langle Y_4^0 \rangle$ moment) was therefore parametrized using two interfering Briet-Wigner amplitudes (for the f and f' mesons) of the following form:

$$f_{BW} = \frac{A(\Gamma_{KK}\Gamma_{\pi\pi})^{1/2}}{M^2 - M_0^2 - iM\Gamma_{tot}}, \tag{5}$$

where A is a constant characteristic of the production amplitude, M is the $K\bar{K}$ effective mass, M_0 the resonance mass, Γ_{KK} and $\Gamma_{\pi\pi}$ the partial widths, and $\Gamma_{tot} = \sum_i \Gamma_i$ the total width of the resonance. The mass dependence of the partial widths was given by[30]

$$\Gamma = \Gamma_0 \frac{(qr)^{2l+1}/D_l}{[(qr)^{2l+1}/D_l]_0}, \tag{6}$$

where Γ_0 is a constant, q is the K momentum in the $K\bar{K}$ rest frame, l is the orbital angular momentum, and the subscript 0 in the denominator indicates that the factor is to be evaluated at the resonant mass. The centrifugal barrier factors are given by

$$\begin{aligned} D_0 &= 1 \\ D_2 &= 9 + 3(qr)^2 + (qr)^4, \end{aligned} \tag{7}$$

where the interaction radius was chosen to be 3.5 GeV^{-1}. Superposition of the f and f' Breit-Wigner amplitudes, f_{BW} and f'_{BW} results in

$$\begin{aligned} f = &[\mathrm{Re}(f_{BW}) + \mathrm{Re}(f'_{BW})\cos\phi - \mathrm{Im}(f'_{BW})\sin\phi] \\ &+ i[\mathrm{Im}(f_{BW}) + \mathrm{Re}(f'_{BW})\sin\phi + \mathrm{Im}(f'_{BW})\cos\phi], \end{aligned} \tag{8}$$

where ϕ is the relative production phase between the two amplitudes. The observable $\langle Y_4^0 \rangle$ was fitted to the square of the function f using a least-squares method. The free parameters of the fit were the relative intensity, $A_{f'}/A_f$, the total width of the f', $\Gamma_{tot}(f')$, and the relative phase, ϕ. The accepted values[31] for the rest of the parameters were used. The results of the least-squares fit were: $\Gamma_{tot}(f') = 92^{+39}_{-22}$ MeV, $\phi = 178 \pm 9°$, and the ratio of the f' intensity to the f intensity is 0.14 ± 0.04. The χ^2 for the fit was 13.5 for 11 degrees of freedom. It should be noted that this value for the total width of the f' meson is significantly higher than the accepted value of 40 MeV of Ref. 31. It is however consistent, within errors, with the width resulting from the effective-mass-spectrometer data.[29] The solid line in Fig. 14 represents the best fit to the data. We conclude that the observed enhancement in the 1400-MeV region is most likely an effect due to f-f' interference.

C. The $f \to K\bar{K}$ branching ratio

In order to determine the $f \to K\bar{K}$ branching ratio correctly, one must take into account the f-f' interference. Using the parameters of the fit determined in the previous section we determine the cross section for the reaction $\pi^- p \to fn$ and the subsequent decay of the f into a $K\bar{K}$ system. Using the intensity ratio and the total D-wave cross section, we find that this cross section is 4.7 ± 0.7 μb at 7.0 GeV/c, and 5.4 ± 0.8 μb at 6.0 GeV/c. These values are corrected for the charged decay mode of the f as well as for the $K_L^0 K_L^0$ mode. After taking into account the fact that our cross sections are for $|t| < 0.2$ (GeV/c)^2 and for $m = 0$, we can use the known cross section for the reaction $\pi^- p \to fn$ with the f decaying into two pions[32] (0.315 ± 0.090 mb at 7.0 GeV/c) to calculate the ratio $R(\Gamma_{f\to K\bar{K}}/\Gamma_{f\to\pi\pi}) = 0.027 \pm 0.009$ and then $R(\Gamma_{f\to K\bar{K}}/\Gamma_{f\to \mathrm{all}}) = 0.023 \pm 0.008$. This branching ratio is consistent, within errors, with the Particle Data Group value of 0.04 ± 0.03 and also with the value 0.024 ± 0.005 from the data of Wetzel *et al.*[13] The result is somewhat below the value of 0.038 ± 0.004 of Pawlicki *et al.*[33]

D. Energy-independent production amplitude analysis

In a previous publication[2] we have shown that a production amplitude analysis of our data shows the presence of a strong S-wave enhancement near 1300 MeV. In this section we discuss the details of that analysis. We then discuss some new results regarding the enhancement.

Understanding the S-wave production of the $K\bar{K}$ system cannot be easily accomplished because there are no observables exclusively dependent on the S-wave amplitude in the manner of the D wave and the $\langle Y_4^0 \rangle$ moment. A complete phase-shift analysis would be impossible because of limited statistics. In the case of quasi-two-body reactions one can obtain information about the production mechanism by an energy-independent production amplitude analysis.[34-36] We have followed mostly the work Ochs in Ref. 36 to analyze our data. In this method the production of the $K\bar{K}$ system of spin l is described by helicity amplitudes $f^l_{\lambda\lambda' m}$ where λ, λ' are the initial and final nucleon helicities and m the $K\bar{K}$ helicity. Then the spin-density matrix is

$$N\rho^{ll'}_{mm'} = \tfrac{1}{2}\sum_{\lambda\lambda'} (f^l_{\lambda\lambda' m})(f^{l'}_{\lambda\lambda' m})^*, \tag{14}$$

where $N = d^2\sigma/dMdt$. (M, t are the $K\bar{K}$ effective mass and the nucleon-nucleon momentum-transfer squared, respectively.) In the following we drop the nucleon helicity indices to simplify the discussion; the inclusion of those indices will be discussed later. The angular distribution $W(\Omega)$ can then be written in terms of the density matrix elements as follows:

$$W(\Omega) = \sum_{ll'mm'} \rho^{ll'}_{mm'}\, Y^m_l(\Omega) Y^{m'}_{l'}{}^*(\Omega). \tag{15}$$

The observables are the moments of the spherical harmonics which are defined as

$$N\langle \mathrm{Re}Y^m_l\rangle = \int W(\Omega)\, \mathrm{Re}Y^m_l(\Omega) d\Omega. \tag{16}$$

In the case of $K^0_S K^0_S$ production only moments with even l are nonvanishing. Assuming that only $l=0$ and $l=2$ $K\bar{K}$ states are produced, these moments are found to be

$$\begin{aligned}
\sqrt{4\pi}\ \langle Y^0_0\rangle &= \rho^{00}_{00} + \rho^{22}_{00} + \rho^{22}_{11} + \rho^{22}_{-1-1} + \rho^{22}_{22} + \rho^{22}_{-2-2},\\
\sqrt{4\pi}\ \langle Y^0_2\rangle &= 2\rho^{02}_{00} + (2\sqrt{5}/7)\rho^{22}_{00} + (\sqrt{5}/7)(\rho^{22}_{11} + \rho^{22}_{-1-1})\\
&\quad - (2\sqrt{5}/7)(\rho^{22}_{22} + \rho^{22}_{-2-2}),\\
\sqrt{4\pi}\ \langle \mathrm{Re}Y^1_2\rangle &= \rho^{02}_{01} - \rho^{20}_{-10} + (\sqrt{5}/7)(\rho^{22}_{01} - \rho^{22}_{-10})\\
&\quad + (\sqrt{30}/7)(\rho^{22}_{12} - \rho^{22}_{-2-1}),\\
\sqrt{4\pi}\ \langle \mathrm{Re}Y^2_2\rangle &= \rho^{02}_{02} + \rho^{20}_{-20} - (2\sqrt{5}/7)(\rho^{22}_{02} + \rho^{22}_{-20})\\
&\quad - (\sqrt{30}/7)\rho^{22}_{-11},\\
\sqrt{4\pi}\ \langle \mathrm{Re}Y^0_4\rangle &= \tfrac{6}{7}\rho^{22}_{00} - \tfrac{4}{7}(\rho^{22}_{11} + \rho^{22}_{-1-1})\\
&\quad + \tfrac{1}{7}(\rho^{22}_{22} + \rho^{22}_{-2-2}),\\
\sqrt{4\pi}\ \langle \mathrm{Re}Y^1_4\rangle &= (\sqrt{30}/7)(\rho^{22}_{01} - \rho^{22}_{-10})\\
&\quad - (\sqrt{5}/7)(\rho^{22}_{12} - \rho^{22}_{-2-1}),\\
\sqrt{4\pi}\ \langle \mathrm{Re}Y^2_4\rangle &= (\sqrt{15}/7)(\rho^{22}_{02} + \rho^{22}_{-20}) - (2\sqrt{10}/7)\rho^{22}_{-11},\\
\sqrt{4\pi}\ \langle \mathrm{Re}Y^3_4\rangle &= -\sqrt{5/7}\,(\rho^{22}_{-12} - \rho^{22}_{-21}),\\
\sqrt{4\pi}\ \langle \mathrm{Re}Y^4_4\rangle &= \sqrt{10/7}\ \rho^{22}_{-22}.
\end{aligned} \tag{17}$$

Equations (17) can then be used to express the moments in terms of the helicity amplitudes. It is convenient to introduce linear combinations of these amplitudes with definite exchange parity,

$$f^l_{m\pm} = \frac{1}{\sqrt{2}}\left[f^l_m \mp (-1)^m f^l_{-m}\right]. \tag{18}$$

An assumption commonly used in π-exchange reactions is that all the unnatural-parity exchange amplitudes are coherent in phase. The same assumption is made here in order to reduce the number of independent variables. (It should be noted that its validity is not assured, especially since production mechanisms other than π exchange may contribute. The existence of a large f signal, however, indicates considerable pion exchange.) Writing the amplitudes[37] as products of a magnitude and a phase factor and using the obvious spectroscopic notation for the magnitudes, Eqs. (17) can be written [using (14) and (18)]

$$\begin{aligned}
\sqrt{4\pi}N\langle Y^0_0\rangle &= S^2 + D_0{}^2 + D_{1+}{}^2 + D_{1-}{}^2,\\
\sqrt{4\pi}N\langle Y^0_2\rangle &= 2SD_0\cos\phi_{SD} + (2\sqrt{5}/7)D_0{}^2\\
&\quad + (\sqrt{5}/7)(D_{1+}{}^2 + D_{1-}{}^2),\\
\sqrt{4\pi}N\langle \mathrm{Re}Y^1_2\rangle &= -\sqrt{2}SD_{1-}\cos\phi_{SD} - (\sqrt{10}/7)D_0D_{1-},\\
\sqrt{4\pi}N\langle \mathrm{Re}Y^2_2\rangle &= -(\sqrt{30}/14)(D_{1+}{}^2 - D_{1-}{}^2),\\
\sqrt{4\pi}N\langle Y^0_4\rangle &= \tfrac{6}{7}D_0{}^2 - \tfrac{4}{7}(D_{1+}{}^2 + D_{1-}{}^2),\\
\sqrt{4\pi}N\langle \mathrm{Re}Y^1_4\rangle &= -(\sqrt{60}/7)D_0D_{1-},\\
\sqrt{4\pi}N\langle \mathrm{Re}Y^2_4\rangle &= -(\sqrt{10}/7)(D_{1+}{}^2 - D_{1-}{}^2).
\end{aligned} \tag{19}$$

So far we have disregarded the nucleon helicities. Each amplitude is really two independent amplitudes, a nucleon helicity-flip and a nonflip amplitude, f^l_{+-m} and f^l_{++m}, respectively.[38] For an experiment involving unpolarized nucleons Eqs. (19) are correct provided it is understood that the nucleon helicities are summed as follows:

$$\begin{aligned}
|f^l_m|^2 &\equiv |f^l_{++m}|^2 + |f^l_{+-m}|^2,\\
\mathrm{Re}(f^l_m f^{l*}_m) &\equiv \mathrm{Re}(f^{l'}_{++m} f^{l*}_{++m} + f^{l'}_{+-m} f^{l*}_{+-m}).
\end{aligned} \tag{20}$$

In π-exchange reactions only spin-flip amplitudes (in the t channel) are allowed. The f production (D wave) is known to be dominated by π exchange. Furthermore, the strong interference pattern in the $\langle Y^0_2\rangle$ moment indicates significant coherence between the S and D waves. This leads us to the assumption that the S wave as well is dominantly spin-flip. Then the seven equations in (19) contain five unknowns. These are the magnitudes of the (spin-flip) amplitudes, S, D_0, D_{1+}, D_{1-}, and the relative phase ϕ_{SD} between the S wave and

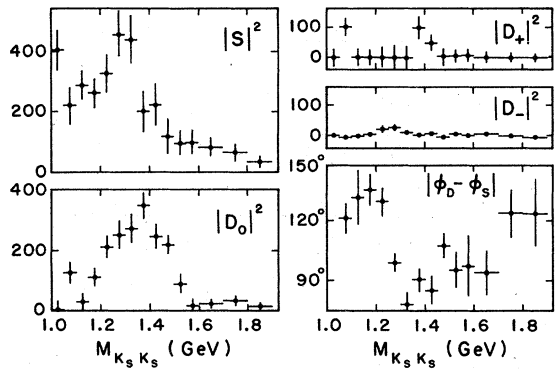

FIG. 17. Results of the energy-independent amplitude analysis for $|t| < 0.2$ (GeV/c)^2.

TABLE VIII. Results of the energy-independent amplitude analysis for $|t| < 0.2\,(\mathrm{GeV}/c)^2$. All amplitudes are expressed in units of events/0.05 GeV.

Mass bin (GeV)	$\lvert S\rvert^2$	$\lvert D_0\rvert^2$	$\lvert D_+\rvert^2$	$\lvert D_-\rvert^2$	ϕ_{SD}	χ^2 [a]
Thresh–1.05	463 ± 72	5 ± 38	2 ± 35	0 ± 1	• • •	0.7
1.05–1.10	221 ± 67	129 ± 39	101 ± 31	−1 ± 3	121 ± 9	7.8
1.10–1.15	291 ± 57	31 ± 29	0 ± 28	0 ± 1	132 ± 14	7.8
1.15–1.20	265 ± 55	112 ± 30	0 ± 25	3 ± 5	135 ± 8	4.5
1.20–1.25	334 ± 73	213 ± 37	0 ± 35	21 ± 10	130 ± 7	2.1
1.25–1.30	463 ± 92	253 ± 50	0 ± 43	23 ± 13	99 ± 5	2.0
1.30–1.35	441 ± 89	275 ± 53	0 ± 39	4 ± 5	78 ± 5	8.3
1.35–1.40	205 ± 85	351 ± 51	100 ± 38	0 ± 1	90 ± 6	1.4
1.40–1.45	225 ± 77	246 ± 46	48 ± 34	7 ± 6	85 ± 6	3.2
1.45–1.50	118 ± 61	217 ± 32	2 ± 29	−5 ± 5	108 ± 10	4.3
1.50–1.55	96 ± 50	93 ± 31	4 ± 22	2 ± 4	96 ± 11	1.2
1.55–1.60	100 ± 44	18 ± 25	7 ± 21	0 ± 2	97 ± 17	0.5
1.60–1.70	83 ± 29	22 ± 17	1 ± 14	4 ± 6	95 ± 11	1.7
1.70–1.80	63 ± 27	35 ± 15	0 ± 13	−2 ± 3	124 ± 13	2.9
1.80–1.90	36 ± 21	15 ± 11	0 ± 11	−4 ± 4	124 ± 18	0.9

[a] For 2 degrees of freedom.

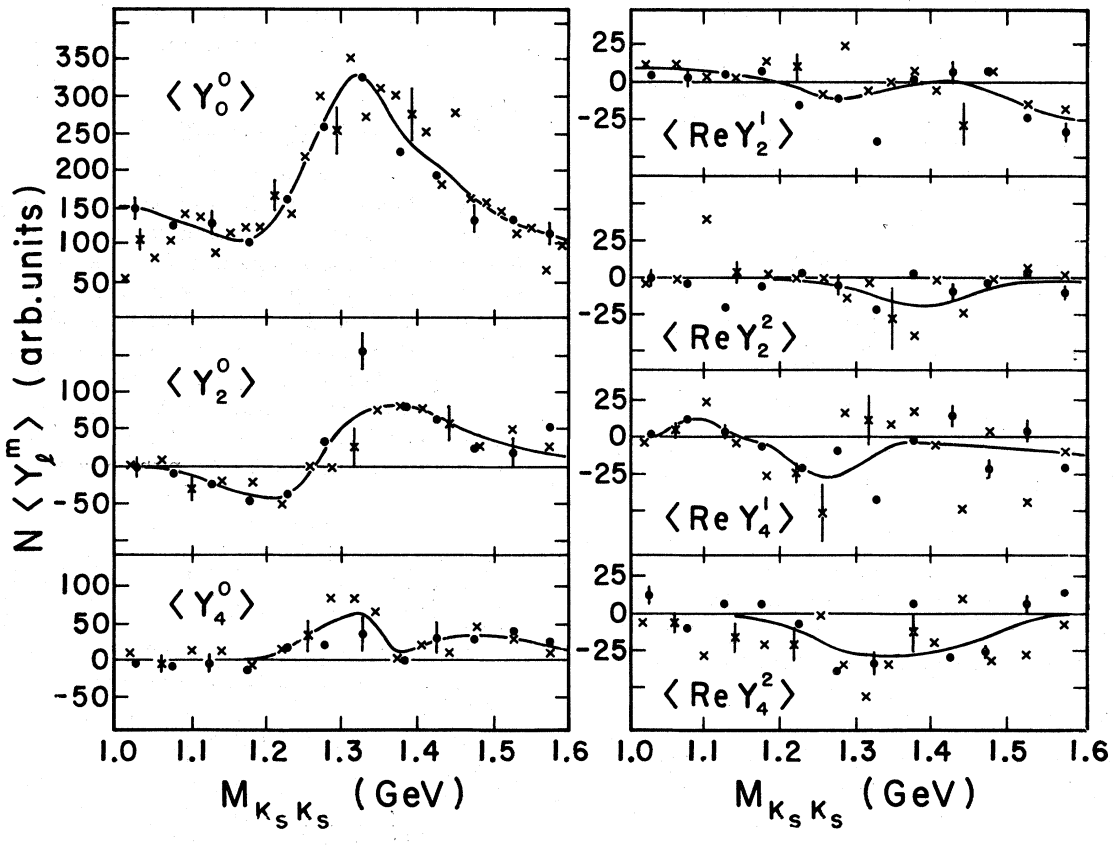

FIG. 18. Unnormalized t-channel moments as a function of the $K_S^0 K_S^0$ effective mass for $0.2 \leq |t| \leq 0.5$ $(\mathrm{GeV}/c)^2$. The dots represent data from this experiment and the crosses are the data of Ref. 13. The smooth curves were used to represent the data for an amplitude analysis of the combined data.

the unnatural-parity D waves.

To summarize, we have assumed the following in order to derive Eqs. (19): (a) no $l \geq 4$ waves are present; (b) no $m = 2$ helicity states are produced; (c) nucleon spin-flip dominance; and (d) phase coherence of the unnatural-parity D waves.

Equations (19) were solved using a least-squares method. The results for $|t| < 0.2$ (GeV/c)^2 are shown in Fig. 17 and are tabulated in Table VIII. We note that S and D_0 dominate although D_{1+} and D_{1-} are not zero everywhere. The S-wave intensity is large at threshold (the S^*), decreases, and then goes through a second maximum in the region near 1300 MeV. The shape is very suggestive of an S-wave resonance on a smoothly falling S-wave background.

Since the statistical accuracy of our data is limited in the higher $|t|$ range $0.2 \leq |t| \leq 0.5$ (GeV/c)^2, we have combined our moments in this t range with the published moments of Ref. 13. In order to combine the data, we have, for each moment, plotted the data from each experiment together and have drawn a smooth curve through the combined data. (This has the effect of requiring the moments to vary smoothly as a function of M_{KK} and thus to ignore any highly energy-dependent effects of the order of 50 MeV or less.) We show in Fig. 18 the combined data and the smooth curve chosen to fit the data. It is clear that the data from the two experiments are generally in agreement (excluding isolated data points) and that the method used gives a good average description of the data. Figure 19 shows $|S|^2$ as a function of M_{KK} for $0.2 \leq |t| \leq 0.5$ (GeV/c)^2. We note that the S^* is still present in this t range although it is significantly suppressed relative to the S-wave enhancement at 1300 MeV. This suggests the production of the latter via a mechanism which falls off more slowly than that of one-pion exchange (which is the S^* production mechanism).

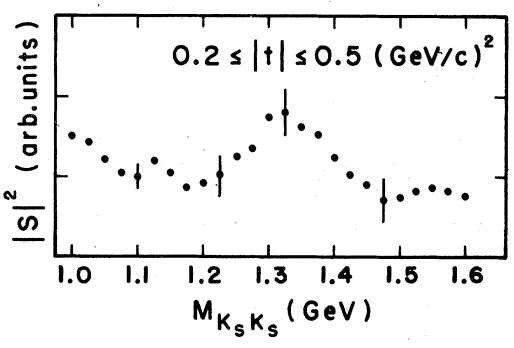

FIG. 19. The S-wave intensity as a function of the $K_S^0 K_S^0$ effective mass for $0.2 \leq |t| \leq 0.5$ (GeV/c)^2 from an amplitude analysis of the data of this experiment combined with that of Ref. 13.

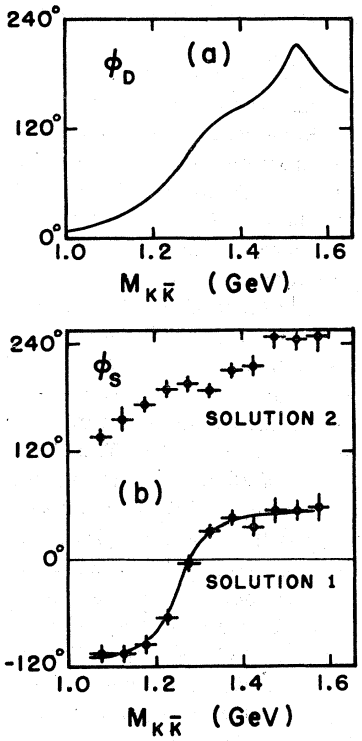

FIG. 20. (a) The D-wave phase as determined by the fit of the $\langle Y_4^0 \rangle$. (b) The two solutions for the S-wave phase derived from the relative phase ϕ_{SD} using the D-wave phase. The solid line represents the fit to the data of a Breit-Wigner phase.

More information on the production mechanism as well as the properties of the enhancement itself can be obtained by studying the phase variation of the S-wave amplitude. The magnitude of the phase difference $|\phi_S - \phi_D|$ is obtained from the amplitude analysis and is shown for the low-t region in Fig. 17. For this t region, we know how the D-wave phase varies with effective mass from our f-f' interference fit. This is shown in Fig. 20(a). We can thus determine the S-wave phase as a function of M_{KK}. The two ambiguous solutions are shown in Fig. 20(b). Solution 1 yields a rapidly varying phase consistent with a narrow Breit-Wigner resonance of mass 1255 MeV and width 79 MeV. The second solution corresponds to a more slowly varying phase. Since the width of the S-wave intensity (especially at high $|t|$, Fig. 19) is inconsistent with the narrow Breit-Wigner interpretation, we conclude that solution 2 is more likely to be correct. In either case, the phase difference between the S wave and the D wave is near 90° in the 1300-MeV region, suggesting non-OPE production for the S wave.

E. S-wave enhancement: Summary and conclusions

Two recent experiments[39,40] have confirmed the observation of an S-wave enhancement coupling to the $K\bar{K}$ state. Here we summarize some of their results before drawing our final conclusions concerning its nature. (A third experiment[13] claims not to observe the effect.)

Cohen *et al.*[39] have performed amplitude analyses of the reactions $\pi^- p \to nK^+K^-$ and $\pi^+ n \to pK^+K^-$ in the t range $|t| < 0.08$ (GeV/c)^2. Their favored solution shows a strong S-wave enhancement near 1300 MeV. In addition, they are able to show that the enhancement is predominantly $I=0$, and they present evidence for its production via one-pion exchange (OPE). Their favored solution has the two S-wave phase variations consistent with ours, and they favor the slower variation because this solution yields an $I=1$ P-wave amplitude consistent with the tail of the ρ^0.

Martin[40] has presented evidence for an S-wave enhancement in the reaction $\pi^- p \to K^- K^0 p$. Such a state obviously has $I=1$ and must therefore be distinct from the state observed by Cohen *et al.* Martin has also analyzed the data of Cohen *et al.* at higher $|t|$ and claims to have evidence for a non-OPE-produced S-wave state at 1300 MeV in their data.

To summarize our data, we observe a strong S-wave enhancement near 1300 MeV which is apparently produced via some non-OPE mechanism. This is based on the observations that the production phase of the state is 90° out of phase with f^0 production, and that the state is produced relatively more strongly as $|t|$ increases than the OPE-produced S^*.

Thus, it would seem from these three experiments that there may actually exist two new S-wave states in the 1300-MeV region. One, the S' would be an $I=0$ state coupling to both $\pi\pi$ and $K\bar{K}$ states (and is thus distinct from the co-called ϵ which is highly elastic). This state dominates the very low $|t|$ data. The second, state the δ', has $I=1$, and is important at higher $|t|$.

If these conclusions are correct, there would clearly be too many states for the conventional P-wave $q\bar{q}$ nonet. In recent years, however, the possibility of the existence of additional mesons (or baryons) consisting of multiquark states has been studied[41,42] by Jaffe. Indeed the description of hadrons in the framework of quantum chromodynamics promises a rich spectrum of multiquark states. Of these states the most accessible to experiment, because of their distinct signatures, are the exotics and kryptoexotics (mesons classifiable as flavor octets or singlets, but consisting of two quarks and two antiquarks, $Q^2\bar{Q}^2$.)

TABLE IX. The two 0^{++} nonets.

Isospin	Name(mass in MeV)	Predominant quark content
0	ϵ(700)	$u\bar{d}d\bar{u}$
0	S^*(993)	$(1\sqrt{2})s\bar{s}(u\bar{u}+d\bar{d})$
1	δ(980)	$u\bar{d}s\bar{s}$
$\frac{1}{2}$	κ(800–1100)	$u\bar{s}d\bar{d}$
0	ϵ'(1300)	$(1/\sqrt{2})(u\bar{u}+d\bar{d})$
0	S'(?)	$s\bar{s}$
1	δ'(1270)	$u\bar{d}$
$\frac{1}{2}$	κ'(1400)	$u\bar{s}$

The majority of the multiquark states would be heavy (mass increasing approximately linearly with the number of quarks), a fact which may account for their apparent absence. Jaffe uses a color-quark-gluon model based on the MIT bag theory[43] to calculate the lowest-lying S-wave $Q^2\bar{Q}^2$ multiplet, a $J^P=0^+$ nonet. He finds the masses of the nonet to be in the neighborhood of 1 GeV. He then argues that the known scalar mesons (ϵ, δ, S^*, κ) belong to this nonet and that the conventional p-wave $q\bar{q}$ nonet lies higher in mass, being approximately degenerate with the tensor nonet. In a later paper[44] he identifies the observed 0^+ mesons as shown in Table IX. Such a scheme could obviously accommodate an additional isovector and two isoscalars as well as an $I=\frac{1}{2}$ doublet. It is then possible, as can be seen in Table IX, that both $I=0$ and $I=1$ resonance S waves may exist in the neighborhood of 1300 MeV.

F. Determination of the $\pi^+\pi^- \to K_S^0 K_S^0$ cross section

In a previous publication[3] we have analyzed these data to obtain the $\pi^+\pi^- \to K_S^0 K_S^0$ scattering cross section. For completeness, we summarize the results of that analysis here.

The procedure used was to divide the 7-GeV data in bins of M_{KK} and t. Mass bins were chosen to be 25 MeV wide, and the t bins chosen were 0.02 (GeV/c)^2. For each mass bin, values of "$t\sigma$" were plotted versus t, and a best fit to a linear dependence going through the origin (the so-called "nonevasive" solution) was determined. In all cases, the data were quite well fitted by a straight line. The extrapolated value at $t=\mu^2$ was then used to determine $\sigma(\pi\pi \to K_S^0 K_S^0)$.

The results are shown in Fig. 21. The cross section has the expected threshold enhancement (the S^*), falls, and then rises in the f^0 region. The solid curve on Fig. 21 shows a two-Breit-Wigner-resonance fit to the data showing that the

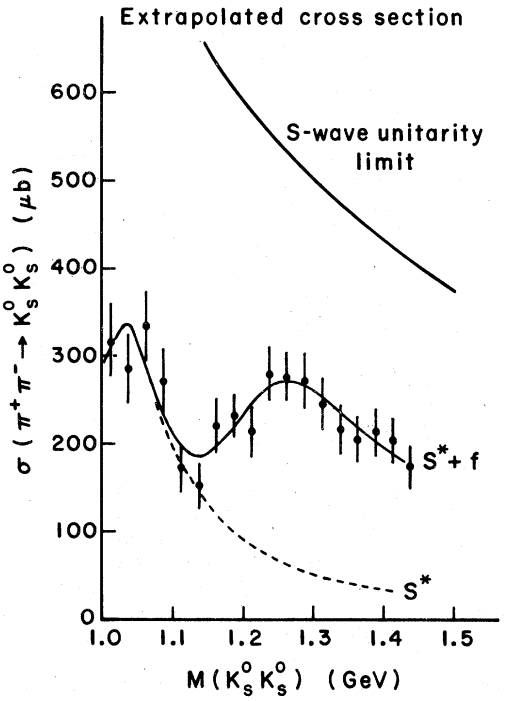

FIG. 21. Values of the cross section for the reaction $\pi^+\pi^- \to K_S K_S$ as a function of the $K_S K_S$ effective mass. Curves are fits to the data assuming S^* and f production.

data are consistent with being dominated by S^* $+f^0$ production. Also shown is the S-wave unitarity limit.

Conclusions reached from the analysis of the data[3] are the following:

(i) The $\pi^+\pi^-$ scattering cross section is well below the S-wave unitarity limit at threshold.

(ii) The magnitude of the cross section at 1270 MeV is consistent with f^0 production and a small tail due to the S^*.

(iii) The $(f^0 \to K\bar{K})/(f^0 \to \text{all})$ branching ratio determined from Fig. 21 is 0.024 ± 0.004, consistent with our result of Sec. V C.

(iv) The $\pi^+\pi^- \to \pi^+\pi^-$ $I=0$, S-wave absorption η_0^0 in the S^* region is $0.80^{+0.09}_{-0.04}$ if the S^* is a standard two-channel Breit-Wigner resonance.

ACKNOWLEDGMENTS

It is a pleasure to thank the scanning and measuring staff at Notre Dame for their dedicated work. The streamer-chamber technicians at Argonne did an excellent job during our running and many ZGS staff members made significant contributions to the success of the experiment. The technical support of R. Erichsen and W. Rickhoff was invaluable. The assistance of A. Baumbaugh, R. Bolduc, P. Higgins, S. Lichtman, and M. Sherlock is gratefully acknowledged. Finally, we would like to acknowledge useful discussions with A. Martin, A. Pawlicki, D. Cohen, R. Diebold, and J. Rosner. The research was supported by the National Science Foundation and the U. S. Department of Energy.

---

†Present address: Fermilab, P. O. Box. 500, Batavia, Illinois 60510. Submitted in partial fulfillment of the requirements for the Ph.D. degree at the University of Notre Dame.

††Present address: E-Systems Inc., P. O. Box 6118, Dallas, Texas 75222.

[1]V. A. Polychronakos, N. M. Cason, J. M. Bishop, N. N. Biswas, V. P. Kenney, W. D. Shephard, and J. M. Watson, Phys. Rev. D 11, 2400 (1975).

[2]N. M. Cason, V. A. Polychronakos, J. M. Bishop, N. N. Biswas, V. P. Kenney, D. S. Rhines, and W. D. Shephard, Phys. Rev. Lett. 36, 1485 (1976).

[3]N. M. Cason, A. E. Baumbaugh, J. M. Bishop, N. N. Biswas, V. P. Kenney, V. A. Polychronakos, R. C. Ruchti, W. D. Shephard, and J. M. Watson, Phys. Rev. Lett. 41, 271 (1978).

[4]A. R. Erwin, G. A. Hoyer, R. H. March, W. D. Walker, and T. P. Wangler, Phys. Rev. Lett. 9, 34 (1962).

[5]G. Alexander, O. I. Dahl, L. Jacobs, G. Kalbfleisch, D. H. Miller, A. Rittenberg, J. Schwartz, and G. A. Smith, Phys. Rev. Lett. 9, 460 (1962).

[6]O. I. Dahl, L. M. Hardy, R. I. Hess, J. Kirz, and D. H. Miller, Phys. Rev. 163, 1377 (1967).

[7]D. J. Crennell, G. R. Kalbfleisch, K. W. Lai, J. M. Scarr, T. G. Schumann, I. O. Skillcorn, and M. S. Webster, Phys. Rev. Lett. 16, 1025 (1966).

[8]W. Beusch, W. E. Fischer, B. Gobbi, M. Pepin, E. Polgar, P. Astbury, G. Brautti, G. Finocchiaro, J. C. Lassalle, A. Michelini, K. M. Terwilinger, D. Websdale, and C. H. Websdale, and C. H. West, Phys. Lett. 25B, 357 (1967).

[9]W. Beusch, A. Birman, D. Websdale, and W. Wetzel, Phys. Lett. 60B, 101 (1975).

[10]T. F. Hoang, D. P. Eartly, J. J. Phelan, A. Roberts, C. L. Sandler, S. Bernstein, S. Margulies, D. W. McLeod, T. H. Groves, N. N. Biswas, N. M. Cason, V. P. Kenney, J. M. Marraffino, J. T. McGahan, J. A. Poirier, and W. D. Shephard, Phys. Rev. Lett. 21, 316 (1968).

[11]T. F. Hoang, D. P. Eartly, J. J. Phelan, A. Roberts, C. L. Sandler, S. Bernstein, S. Margulies, D. W. McLeod, T. H. Groves, N. N. Biswas, N. M. Cason, V. P. Kenney, J. M. Marraffino, J. T. McGahan, J. A. Poirier, and W. D. Shephard, Phys. Rev. 184, 1363 (1969).

[12]J. M. Marraffino, Ph.S. thesis, University of Notre Dame, 1969 (unpublished).

[13]W. Wetzel *et al.*, Nucl. Phys. B115, 208 (1976).

[14]P. S. Sokolsky, Ph.D. thesis, University of Illinois, 1973 (unpublished).

[15]A. Abashian, N. Beamer, R. Eisenstein, J. D. Hansen, W. Mollet, G. R. Morris, T. O'Halloran, J. R. Orr,

D. S. Rhines, P. Schultz, P. Sokolsky, S. J. Prunster, J. M. Watson, and M. Buttram, Nucl. Instrum. Methods 115, 445 (1974).
[16]Proceedings of the First International Conference on Streamer Chamber Technology, 1972 [ANL Report No. ANL-8055 (unpublished)].
[17]J. M. Watson, ANL Report No. ANL/HEP 7238 (unpublished).
[18]This was effectively the accuracy to which the magnetic field could be controlled during the runs.
[19]The program VERTEX was developed by J. D. Hansen at the University of Illinois at Urbana-Champaign. It was adapted at Notre Dame for the double-V topology.
[20]The probability density function for a proper lifetime τ was taken to be proportional to $\exp(-\tau/\tau_0)$ where τ_0 is the mean proper lifetime of the K_S^0 (0.886×10^{-10} sec).
[21]Since the anticounters inside the streamer chamber were not optically isolated from one another, but were inside a common light-tight box, scintillation in one counter could conceivably be observed by a second counter. If $A1$ detects any light from $A2$ or $A3$, it vetoes a beam count and effectively increases the cross section. An upper limit of 10% beam loss was measured. It is not known how much of the 10% was due to this effect and how much was due to beam halo which would not affect the cross section. Therefore, a correction factor of 0.95 ± 0.05 is used.
[22]S. B. Treiman and C. N. Yang, Phys. Rev. Lett. 8, 140 (1962).
[23]C. Zweig, CERN Reports Nos. TH401, 1964, TH412, 1964 (unpublished).
[24]J. Iizuka, Prog. Theor. Phys. Suppl. 37–38, 21 (1966).
[25]H. J. Lipkin, Phys. Rev. 176, 1709 (1968).
[26]A. J. Pawlicki, D. S. Ayres, R. Diebold, A. F. Greene, S. L. Kramer, and A. B. Wicklund, Phys. Rev. D 12, 631 (1975).
[27]M. J. Emms *et al.*, Phys. Lett. 58B, 117 (1975).
[28]M. J. Corden *et al.*, University of Birmingham report (unpublished).
[29]A. J. Pawlicki, D. S. Ayres, D. Cohen, R. Diebold, S.L. Kramer, and A. B. Wicklund, Phys. Rev. Lett. 37, 971 (1976).
[30]Angela Barbaro-Galtieri, in *Advances in Particle Physics*, edited by R. L. Cool and R. E. Marshak (Wiley, New York, 1968), Vol. 2.
[31]Particle Data Group, Phys. Lett. 50B, 1 (1974).
[32]E. Bracci, J. P. Droulez, E. Flaminio, J. D. Hansen, and D. R. O. Morrison, CERN Report No. CERN/HERA 72-1, 1972 (unpublished).
[33]A. J. Pawlicki *et al.*, Phys. Rev. D 15, 3196 (1977).
[34]P. Estabrooks and A. D. Martin, Phys. Lett. 41B, 350 (1972).
[35]B. Hyams, C. Jones, P. Weilhammer, W. Blum, H. Dietl, G. Grayer, W. Koch, E. Lorenz, G. Lutjens, W. Manner, J. Meissburger, W. Ochs, and U. Stierlin, Nucl. Phys. B100, 205 (1975).
[36]W. Ochs, Nuovo Cimento 12A, 724 (1972).
[37]Helicity-two amplitudes are omitted in the following since both $\langle Y_4^3 \rangle$ and $\langle Y_4^4 \rangle$ moments were found to be consistent with zero.
[38]P. Estabrooks, A. D. Martin, G. Grayer, B. Hyams, C. Jones, P. Weilhammer, W. Blum, H. Dietl, W. Koch, E. Lorenz, G. Lutjens, W. Manner, J. Meissburger, and U. Stierlin, in π-π *Scattering*—1973, proceedings of the International Conference on π-π Scattering and Associated Topics, Tallahassee, edited by P. K. Williams and V. Hagopian (AIP, New York, 1973), p. 37.
[39]D. Cohen, in *Experimental Meson Spectroscopy, 1977*, proceedings of the Fifth International Conference, Boston, edited by E. von Goeler and R. Weinstein (Northeastern Univ. Press, Boston, 1977), p. 238.
[40]A. D. Martin, in *Phenomenology of Quantum Chromodynamics*, proceedings of the XIIth Rencontre de Moriond, Les Arcs, 1978, edited by J. Trân Thanh Vân (Editions Frontières, Dreux, 1978), p. 363; A. D. Martin *et al.*, Phys. Lett. 74B, 427 (1978).
[41]R. L. Jaffe, Phys. Rev. D 15, 267 (1977).
[42]R. L. Jaffe, Phys. Rev. D 15, 281 (1977).
[43]A. Chodos *et al.*, Phys. Rev. D 9, 3471 (1974).
[44]R. L. Jaffe, in *Phenomenology of Quantum Chromodynamics* (Ref. 40).